Global Scientific JOURNALS
GSJ: Volume 10, Issue 9, September 2022, Online: ISSN 2320-9186
www.globalscientificjournal.com

Measuring Lithium solubility in LiFePO4 grains boundaries After oxidation using atom probe tomography

Abdul Wahab Qurashi[1],Dr Guido Schmitz[1]
[1] Department of Material Sciences, University of the Stuttgart Germany.

Corresponding Author: abdulwahab312@gmail.com

Abstract

Poor oxidation resistance is a key contributor to material failure within extreme environments. Understanding oxygen solubility is important for computation aided design of new battery electrode material $LiFePO_4$ especially when Lithium is important to define the suitability of electrode material. Lithium mobility within compound, such as $LiFePO_4$, has been studied using Atom Probe Tomography *(APT). APT* is the only technique offering both a high chemical sensitivity *(<10 ppm)* and resolution *(<1 nm)* allowing for a composition measurement within nanometers of the oxide/metal interface. *APT* was employed to measure the Lithium and oxygen content at different depths from the oxide/metal interface as well as on grain boundaries at different temperature and check the mobility of lithium on grain boundaries. The results reveal *<10 s* of ppm oxygen solubility within $LiFePO_4$ at all depths and *100 s* of ppm Lithium within *GBs*.

Keywords: Lithium iron phosphate, mobility, UV laser, atom probe tomography.

Introduction

The demand for efficiency enhancements and emission reductions in the power generation and transportation industries is driving operating temperatures higher than before *[1,2]*. Enabling multiple energy sources requires new high temperature sustainable materials that can withstand increasingly harsher environments as well as rest to degradation *[3]*. Consequently, high temperature erosion/corrosion is amongst one of the life- limiting degradation mechanisms that must be addressed during selection of electrode material in batteries.

Recent progress in computation hardware and software has enabled computation aided compound design to be an efficient and effective method for designing new compounds for batteries *[4–9]*. However, modeling of new materials in atom probe tomography is extremely challenging due to the local nature of the processes that can be influenced by a combination of factors. Although there has been significant progress in predicting diffusion of lithium in grain boundaries of lithium iron phosphate *[6,10,11]*, there is no comprehensive model to predict the accurate diffusion of lithium ions on grain boundaries of compound at different temperature*[12]*. Mobility of Lithium on grain boundary depends on the oxide thermodynamic stability during heating, iron mobility, chromium oxidation, temperature, pressure of chamber, and oxide

Particle nucleation density *[13,14]*. Quantitative information on each of these parameters is essential to check the mobility of lithium ions on grain boundaries between the interphase. Yet, the experimental determination of hydrogen has received limited attention because of challenges with detecting light elements in low concentration with high spatial resolution *[15–18]*.

There are several studies that measured iron solubility in $LiFePO_4$, including those by Seybolt and Fullman *[15]*, Alcock and Brown *[19]*, and Park and Altstetter *[16]*. These three pivotal studies showed the mobility of Lithium ion in $LiFePO_4$ subject to the temperatures ranging from *700–1200 °C [20]*. The $LiFePO_4$ was polycrystalline in these studies making the delineation of *GB* effects impossible.

Results and Discussion

Here, we have employed *APT* to understand the percentage of elements and mobility of Lithium ion in $LiFePO_4$ subject to the temperature. *APT* is a direct projection microscopy technique with sub nanometer resolution *<10 ppm* sensitivity *[24–28]*. Unfortunately, oxygen and hydrogen quantification is challenging because some field evaporated oxide molecules can be undetectable due to multi-hit detection events or molecular ion disassociation after field evaporation *[29–32]*. On the other hand, the detection of residual oxygen and hydrogen ions from the ultra-high vacuum *(~10–11 Torr)* analysis chamber can increase the measured oxygen concentration. Despite these challenges, dissolved oxygen and lithium diffusion within nanometers of the oxide scale interface and within *GBs* was measured with *APT*. This information can be used to improve computational models and accelerate material development designed for extreme environments.

Table 1: Mass spectrum peaks of un-annealed sample.

m/z[Da]	Identity	m/z[Da]	Identity	m/z[Da]	Identity
1	H^{+1}	33-34	PH_3^{+1}	71.8-72.2	$LiP_2H_3^{+1}$
6-7	Li^{+1}	43.8-44..2	FeO_2^{+1}	84-86	CrO_2^{+1}
16-16.2	O^{+1}	46.9-47.2	PO^{+1}		
17-17.2	OH^{+1}	52-54	Cr^{+1}		
18-18.2	H_2O^{+1}	56-58.5	Fe^{+1}		
25-27	Cr^{+2}	62.8-63.2	P_2H^{+1}		
27.5-28.5	Fe^{+2}	64	$P_2H_2^{+1}$		
31	P^{+1}	65	$P_2H_3^{+1}$		
31.5-32	O_2^{+1}	66	$P_2H_4^{+1}$		
33	PH_2^{+1}	68	$FePO_4^{+1}$		

The chemical compositions of the studied compound are given in Table 1 using inductively coupled ultra violet laser in the presence of high field.

APT specimens were fabricated with an *FEI Nova 200* dual beam scanning electron microscope (SEM)/focused ion beam (FIB) instrument using the method described by Thompson et al. *[33]* as shown in Figure 1.

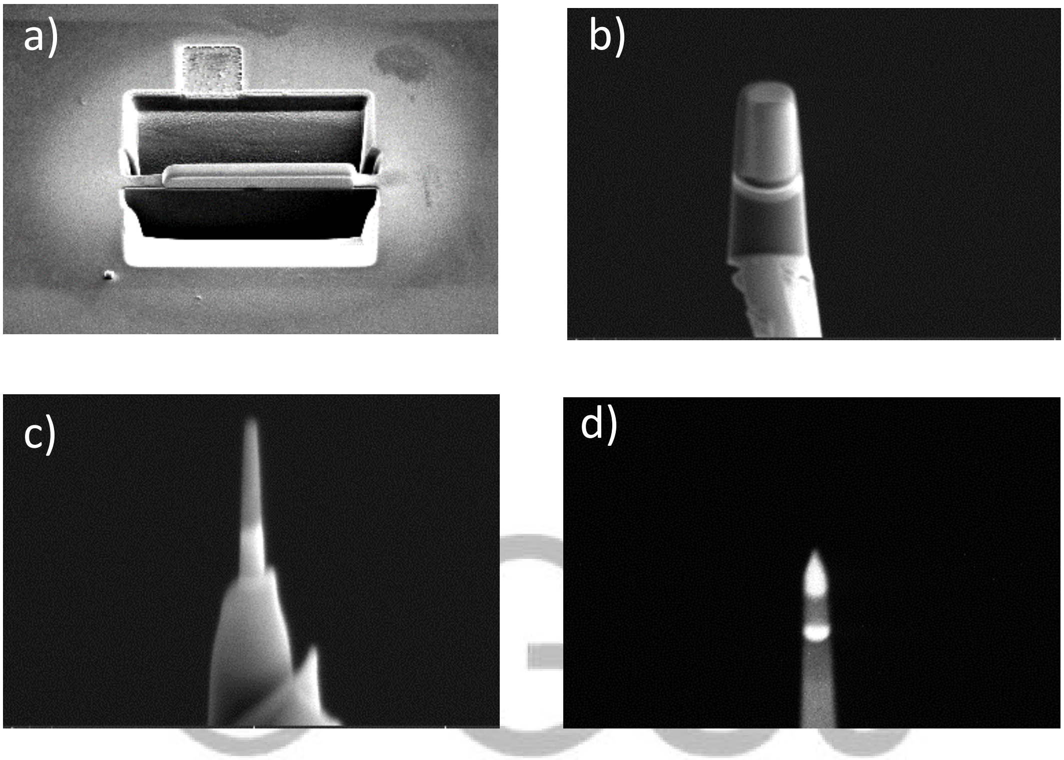

Figure 1: Lift out for the site-specific specimen preparation. First selection of feature of interest and put this on tungsten post and the next stage is the milling of lifted portion to make it sharp for Atom probe measurement.

The *APT* experiments were run using a *CAMECA LEAP 4000XHR* in laser mode with a *30 K* base temperature, a *60–70 pJ* laser power, *a 0.2%* detection rate, and a *200 kHz* pulse repetition rate. The APT results were crytallographically calibrated *[34]*, and analyzed using *CAMECA's IVAS 3.8 software*. The misorientation of the *APT* dataset grain boundaries were measured using the protocol outlined by Breen et al. *[35]*. The error presented in the proximity histograms and *Table 2* is the standard error *[25]*. This value does not represent the total error because phenomena such as residual oxygen in the vacuum chamber and preferential loss of oxygen can add to error but is difficult to quantify.

Table 2: Mass spectrum peaks of un-annealed sample.

Location	Sample	Oxygen measurement
^{18}~10 µm from int.	O-Ni	16±1
>1 mm from int.	16O-Fe200	26±2
Noise	N/A	~10

APT atom maps for the Lithium/metal interface for $LiFePO_4$ are shown in *Fig. 2*. Much care needs to be taken when determining the low metal oxygen content because there are mass spectral peak overlaps that need to be considered. $^{18}O_2$ and $^{16}O_2$ oxidation experiments were conducted to differentiate residual *APT* chamber vacuum gas from oxygen within the specimen and to determine the molecular state oxygen is detected. Mass spectra from volumes in the *APT* data are displayed in *Fig. 2*.

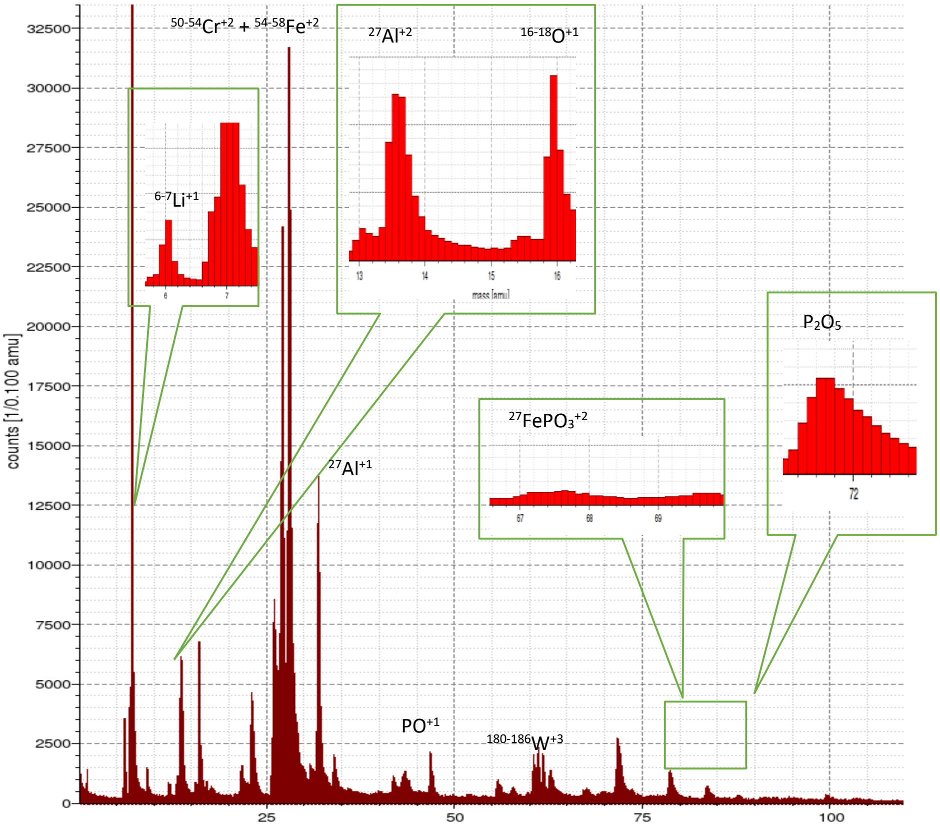

Figure 2: Typical mass spectrum of 150nm sputter LFP with a 20nm of Aluminum as a blanket on top of W tip. Different peak on different Da values are marked with their oxidative states.

One of the features of Lithium iron phosphate after a annealing is the number of peaks in mass spectrum *(Fig 2)* as compare to un-anneal sample *Table 1*. In the case of annealing, a blanket of 20*nm* of Aluminum is used to protect the Lithium iron phosphate from evaporation during annealing. Aluminum on *LFP* is also used to protect the tips from charging. However, the compound formation in the annealed sample is larger and it is validated from the mass spectrum. The compound of Lithium, iron and phosphorous is determined by the position of the respective peaks. However, the composition of the elements and compounds are calculated by integrating the area of the respective peaks. For the full reconstruction of the obtained dataset, the resulting mass spectrum is identified according to the following mass window of anneal sample *(Table:3).*

Table 3: Mass spectrum peaks of anneal sample.

m/z[Da]	Identity	m/z[Da]	Identity	m/z[Da]	Identity
1	H^{+1}	26.8-27.5	Al^{+1}	71.5-72.5	$P_2O_5^{+2}$
5.8-7.5	Li^{+1}	27.5-29.5	Fe^{+2}	77.9-80	$LiFePO_4^{+2}$
8.8-9.2	LiH_2^{+1}	29.5-31.5	P^{+1}	83-84	$Li_3P_2O_5H_4^{+2}$
11.8-12.2	C^{+1}	31.5-32.5	O_2^{+1}		
12.8-13.2	CH^{+1}	33.5-34.5	PH_3^{+1}		
13.4-13.8	Al^{+2}	41.6-43.5	$LiPH_5^{+1}$		
15.8-16.5	O^{+1}	46.5-47.2	PO^{+1}		
21.2-22	AlO^{+1}	54-58	Fe^{+1}		
22-23.5	LiO^{+1}	60-62	W^{+3}		
25-26.5	Cr^{+2}	66.5-72.2	$FePO_3^{+2}$		

One of the big advantages of *APT* is its ability to identify all the atomic species with high accuracy. The probability of detecting hydrogen (Light element) and on the other side uranium (Heavy element) is the same. Peaks appear in the annealed sample as shown in the mass spectrum *Fig 2*. Peaks in *Fig 2* are not sharp, it can be due to different vaporization rate of elements or may be due to formation of molecules during flight length. However, it is clear that some peaks *of* LiH_2^{+1}, AlO^{+1}, PH_3^{+1} PO^{+2}, $LiPH_5^{+1}$, $FePO_2H_2^{+2}$, $FePO_3^{+2}$,$P_2O_5^{+2}$, $LiFePO_4^{+2}$ and $Li_3P_2O_5H_4^{+2}$ appear additionally in comparison to the un-anneal sample at *8.8-9.2 , 21.2-22 , 33.5-34.5, 46.5-47.2 , 41.6-43.5 , 60-6.90 , 66.5-69 , 71.5-72.5 , 77.9-80* and *83-84 Da* respectively . Sometimes a controversy in peak identification can occur due to overlapping peaks and it's a difficult to identify the right positions of isotopes. For instance, *100%* alignment of peaks is difficult in this measurement and uncertainty of *0.1- 0.2 Da* is still present in the mass spectrum. So, for instance, the multiple peaks between *11-32* are mostly just pure elements and diatomic compounds can assign as C^{+1},CH^{+1},Al^{+2},O^{+1},AlO^{+2},PO^{+2},Cr^{+2},Al^{+1},Fe^{+2},P^{+1}, and O_2^{+1}. However, a semi-empirical method might be effective for this case because unfortunately there is no precise mathematical deconvolution.

In comparison to the sample prepared by a milling process in the Focused ion beam microscopy, the peak of Aluminum is missing in the mass spectrum *Fig 2*. Because the Aluminum layer on the top of the tip was removed during milling process in the Focused ion beam microscopy. However, the peaks from *11-31* cannot ascribe to as complex compounds of lithium and phosphorus. Moreover, Li^{+1} have the maximum intensity which lies from *6-7 Da* and counts of its compounds $LiPH_5^{+1}$, Li_3Ga, $FePO_3$, $LiFePO_4$ and $Li_3P_2O_5H_4$ are very low. These complex compounds are homogeneously distributed within the layer of *LFP*.

Therefore, it can be said that the incoming events are not from localized features within the tip. During the *APT* measurement of annealed *LFP*, some important problems are found and this study tries to solve these problems. Problems are listed below:

Use the layer of Chromium *(4nm)* between Tungsten and Lithium iron phosphate to enhance adhesion. Loss of Lithium iron phosphate during annealing from tip surface and it is avoided by using a *20nm* thick layer of aluminum on top of the tip.

Decrease the power of the laser down to *13-15mW* for the un-annealed tip and *17-20mW* for the annealed tip during measurement of *APT*.

Increase the temperature of the tip holder up to *83K* to support the evaporation of material during *APT* measurement.

Fixing the peaks on correct position during reconstruction is a major issue for the annealed case, some peaks are fixed on right position but some are still shifted from integral and half-integral *Da* values with an uncertainty of *0.1-0.2 Da*.

Typical mass spectrum recorded with the sample prepared by the Focused beam, measured with UV laser assisted field evaporation is shown in *Fig 2*. Numerous peaks in both spectra correspond to PO_x complexions, these ions are common in the mass spectrum of tip developed by Filed ion microscopy and tip prepared with milling process in Focused ion beam microscopy. However, peaks of PO_x complexions are common for phosphorus-containing compounds *[39]*. While it is observed that Fe^{+1}, Fe^{+2} and Li^{+1} appear predominantly common as elemental ions in both measurements. Obvious differences are present after comparing both mass spectra. Numerous complexions of P_xH_x with normal UV assisted laser of *20mV* are observed in the mass spectrum (Tip prepared by FIB) *e.g* PH_2^{+1}, PH_3^{+1}, $P_2H_3^{+1}$ and $P_2H_5^{+1}$ at *32.9-34.2, 33.8-34.2, 64.9-65.5,* and *66.8-67.5*. Oppositely, there is no identification of P_xH_x complex in the mass spectra of tip developed by Field ion microscopy *(Fig 2).*

Integrating the peaks on the basis of the mass spectrum in *Fig 2* gives the elemental composition of different elements. However, the relative ratio of the individual elements *(Li, Fe, P, Cr and O)* along the diagonal of tip is represented as a composition profile in *Fig 3*.

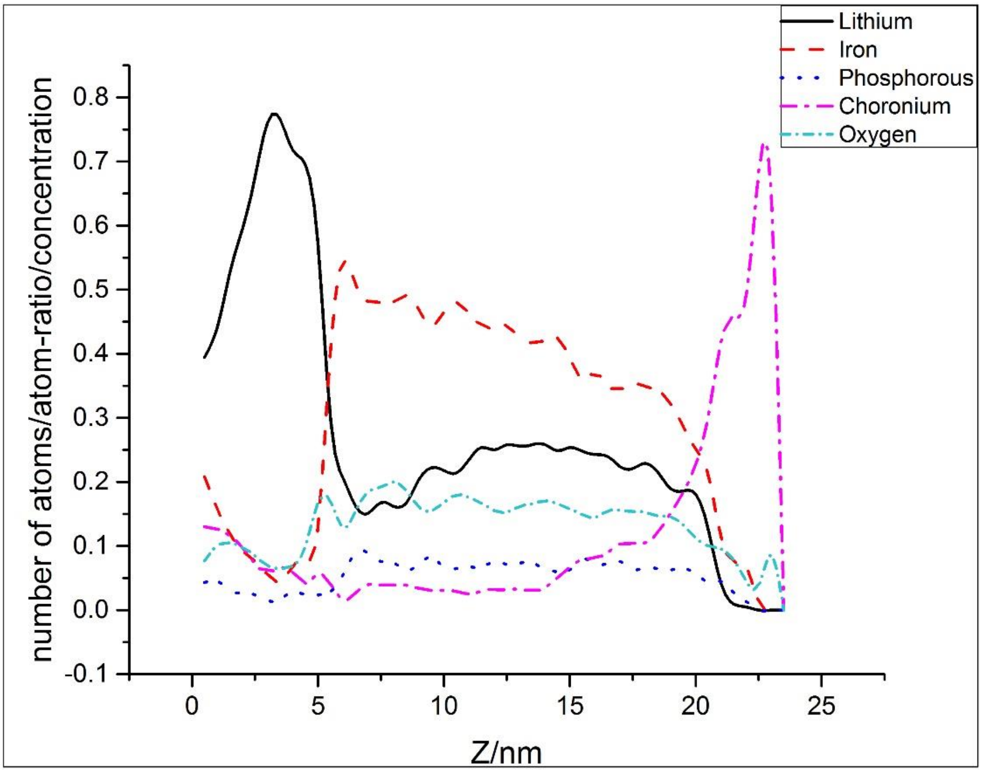

Figure 3: Composition profile of Li, Fe, P and O along the measurement direction from bottom to apex of tip.

Moreover, it can clearly identify that the band region is located at one side of the cylindrical (left top side of Cylinder) *Fig 3* which is enriched with *40 %* of pure lithium, *22 %* of iron, *15%* chromium, *5 %* of phosphorus and *8%* of oxygen representing in *Fig 3* (at zero distance from the tip). The corresponding composition profile indicates that *Li* is diffusing to the surface (28% of lithium) and remaining other elements *Cr*, *Fe* and *P* are spread in the whole tip. Oppositely, the amount of Chromium is maximum at the end corner of measured tip because it's the intermediate layer between LFP and tungsten (Bottom right side in the reconstruction of the tip *Fig 3*.

Table 4: Composition of Li, Fe, P, Cr and O of un-annealed sample.

	Li	**Fe**	**P**	**Cr**	**O**
Absolute quantity	1298849	1194274	3910	190558	404391
Relative percentage	42.00	38.62	0.126	13.07	6.16

References

[1] D. Shifler, Mater. High Temp. 32 (1–2) (2015) 148–159.

[2] M. Schütze, W.J. Quadakkers, Oxid. Metals 87 (5) (2017) 681–704.

[3] J. Anderson, D. Rode, H.B. Zhai, P. Fischbeck, Energ. Policy 148 (2021).

[4] Y. Yamamoto, G. Muralidharan, M.P. Brady, Scr. Mater. 69 (11–12) (2013) 816–819.

[5] R. Pillai, K. Kane, M. Lance, B.A. Pint, Computational methods to accelerate de- velopment of corrosion resistant coatings for industrial gas turbines, Superal- loys (2020) 2020.

[6] A. Chyrkin, R. Pillai, H. Ackermann, H. Hattendorf, S. Richter, W. Nowak,

[7] D. Gruner, W.J. Quadakkers, Corros. Sci. 96 (2015) 32–41.

[8] G.B. Olson, C.J. Kuehmann, Scr. Mater. 70 (2014) 25–30. [8] G.B. Olson, Scr. Mater. 70 (2014) 1–2.

[9] G.B. Olson, Science 288 (5468) (2000) 993.

[10] R. Duan, A. Jalowicka, K. Unocic, B.A. Pint, P. Huczkowski, A. Chyrkin, D. Grüner,

[11] R. Pillai, W.J. Quadakkers, Oxid. Metals 87 (1) (2017) 11–38.

[12] B.A. Pint, R. Pillai, M.J. Lance, J.R. Keiser, Oxid. Metals 94 (5–6) (2020) 505–526.

[13] D.J. Young, High Temperature Oxidation and Corrosion of Metals, Elsevier, Ox- ford, 2008.

[14] C. Wagner, Zeitschrift fur Elektrochemie 63 (7) (1959) 772–790. [14] C. Wagner, J. Electrochem. Soc. 99 (10) (1952) 369–380.

[15] A.U. Seybolt, R.L. Fullman, JOM 6 (5) (1954) 548–549.

[16] J.W. Park, C.J. Altstetter, Metallurgical Transactions A 18 (1) (1987) 43–50.

[17] J.H. Swisher, Turkdoga. Et, Trans. Metal. Soc. Aime 239 (4) (1967) 426 -&.

[18] D. Jullian, J.Q. Zhang, D.B. Hibbert, D.J. Young, J. Alloys Compd. 732 (2018) 646–654.

[19] C.B. Alcock, P.B. Brown, Metal Sci. J. 3 (1) (1969) 116–120.

[20] A. Sieverts, Zeitschrift für Metallkunde 21 (1929) 37–46.

[21] S. Perusin, D. Monceau, E. Andrieu, J. Electrochem. Soc. 152 (12) (2005) E390.

[22] D.A. Woodford, R.H. Bricknell, Metall. Mater. Trans. A 12 (8) (1981) 1467–1475.

[23] R.H. Bricknell, D.A. Woodford, Metal. Trans. A 12 (3) (1981) 425–433.

[24] D.J. Larson, T. Prosa, R.M. Ulfig, B.P. Geiser, T.F. Kelly, New York, US: Springer Science (2013).

[25] M.K. Miller, Atom Probe Tomography, Springer US, Boston, MA, 2000.

[26] F. De Geuser, B. Gault, Acta Mater. 188 (2020) 406–415.

[27] B.M. Jenkins, F. Danoix, M. Gouné, P.A.J. Bagot, Z. Peng, M.P. Moody, B. Gault, Microsc. Microanal. 26 (2) (2020) 247–257.

[28] D. Haley, A.J. London, M.P. Moody, Microsc. Microanal. 26 (5) (2020) 964–977.

[29] B. Gault, D.W. Saxey, M.W. Ashton, S.B. Sinnott, A.N. Chiaramonti, M.P. Moody, D.K. Schreiber, New J. Phys. 18 (3) (2016) 033031 -17.

[30] A. Devaraj, R. Colby, W.P. Hess, D.E. Perea, S. Thevuthasan, J. Phys. Chem. Lett. 4 (6) (2013) 993–998.

[31] R. Kirchhofer, D.R. Diercks, B.P. Gorman, J.F. Ihlefeld, P.G. Kotula, C.T. Shelton, G.L. Brennecka, J. Am. Ceramic Soc. 97 (9) (2014) 2677–2697.

[32] R. Kirchhofer, M.C. Teague, B.P. Gorman, J. Nucl. Mater. 436 (1) (2013) 23–28.

[33] K. Thompson, D. Lawrence, D.J. Larson, J.D. Olson, T.F. Kelly, B. Gorman, Ultra- microscopy 107 (2–3) (2007) 131–139.

[34] B. Gault, M.P. Moody, F. de Geuser, G. Tsafnat, A. La Fontaine, L.T. Stephenson, D. Haley, S.P. Ringer, J. Appl. Phys. 105 (3) (2009) 034913.

[35] A.J. Breen, K. Babinsky, A.C. Day, K. Eder, C.J. Oakman, P.W. Trimby, S. Primig, J.M. Cairney, S.P. Ringer, Microsc. Microanal. 23 (2) (2017) 279–290.

[36] O. Dyck, D.N. Leonard, L.F. Edge, C.A. Jackson, E.J. Pritchett, P.W. Deelman, J.D. Poplawsky, Adv. Mater. Interfaces 4 (21) (2017).